

PAPER

IR-range photoinduced diode effect in the manganese-substituted bismuth ferrite films

To cite this article: S S Aplesnin *et al* 2019 *Semicond. Sci. Technol.* **34** 095007

View the [article online](#) for updates and enhancements.





IOP | ebooks™

Bringing you innovative digital publishing with leading voices to create your essential collection of books in STEM research.

Start exploring the collection - download the first chapter of every title for free.

IR-range photoinduced diode effect in the manganese-substituted bismuth ferrite films

S S Aplesnin^{1,2} , V V Kretinin², A N Masyugin², O B Romanova^{1,3} ,
M N Sitnikov², O B Begisheva², A I Galyas⁴, O F Demidenko⁴ and
K I Yanushkevich⁴

¹Kirensky Institute of Physics, Federal Research Center KSC SB RAS, Krasnoyarsk, Russia

²Reshetnev Siberian State University of Science and Technology, Krasnoyarsk, Russia

³Siberian Federal University, Krasnoyarsk, Russia

⁴Scientific-Practical Materials Research Center NAS of Belarus, Minsk, Belarus

E-mail: rob@iph.krasn.ru

Received 17 April 2019, revised 22 June 2019

Accepted for publication 11 July 2019

Published 30 July 2019



Abstract

The photoinduced diode effect has been found in $\text{BiMn}_x\text{Fe}_{1-x}\text{O}_3$ ($0 < X < 0.15$) films in the near-infrared and violet spectral ranges in a wide temperature interval. The dependences of the diode effect on temperature, wavelength, and illumination power have been established. The mechanism of the ferroelectric diode has been determined using its I - V characteristics at different illumination powers, optical spectra, far-infrared absorption spectra, and electric polarization hysteresis. The interplay between the photodiode effect and conductivity mechanism has been elucidated. The model of strong Coulomb potential fluctuations and quantum well asymmetry caused by the electric polarization in the film and difference between the times of carrier thermalization and recombination of electrons and holes is proposed.

Keywords: multiferroic, films, diode effect, polarization, I - V characteristics, optical absorption

1. Introduction

The interplay between the characteristics of electron transport and ferroelectric polarization has been seldom studied because of the formation of domain walls [1–3] and crystallographic defects. Multiferroic materials [4, 5] can contain domains of two interrelated types: ferroelectric [6, 7] and magnetic [8, 9]. Bismuth ferrite is a high-temperature multiferroic [10–12], in which the photocurrent direction depends on the electric polarization direction [13, 14]. Ferroelectric domain walls can be manipulated by changing the angle of polarization of a coherent light source and electric-field switching [15]. The conductivity of magnetic and ferroelectric domain walls is higher than the conductivity of a domain by a few orders of magnitude and the activation energy in the electron excitation spectrum is lower than in the bulk by 10%–20% [16, 17]. The photoinduced carriers compensate the electric polarization field and degrade the ferroelectric properties. In ferroelectrics, the band gap (the gap in the electron excitation spectrum) is larger by 3 eV; [18, 19] in bismuth ferrite, the gap is located in the optical range [20, 21]

and, upon substitution of 3d metals, shifts to the near-infrared (IR) range [22, 23].

The creation of multiferroics with a narrow gap in the electron excitation spectrum and high absorption of the electromagnetic radiation in the visible and IR ranges is promising for new optoelectronic applications, attenuators, sensors, and memristor devices [4, 10, 24]. The characteristics of the multiferroics are not inferior to oxide semiconductors such as SnO_2 [25], ZrO_2 [26], ZnO [27].

Substitution of manganese ions for iron ions in a concentration of $X = 0.2$ leads to a decrease in the optical gap to 1.5 eV; [28] substitution of cobalt ions in a concentration of $X = 0.1$ decreases the gap to 1.6 eV [29]. Substitution of 3d elements changes the magnetic structure and gives rise to a hysteresis with the formation of domains and domain walls, which lead to an additional ferroelectric polarization.

Manganese ferrite has a gap of 0.46 eV in the optical excitation spectrum [30]. During film deposition, oxygen vacancies and iron ion valence fluctuations occur, since the gap in the electron excitation spectrum of the iron oxide lies between 2.05–2.4 eV [31]. In the manganese-substituted

bismuth ferrite, the Coulomb potential fluctuations in the range of 0.5–1 eV occur in the ideal crystal structure, which originate from the stochastic distribution of Mn^{3+} ions over the crystal lattice sites. The presence of defects in the anion sublattice will lead to the iron ion valence fluctuations and enhance the dispersion of the potential and energy of the electron transition from the bound to delocalized state on a certain scale. The electric polarization will result in the asymmetry of quantum well and induce the random potential gradient. Thus, upon absorption of light quanta, nonequilibrium electrons and holes appear spatially separated, which slows down their recombination. In this case, the electric-field-driven diode effect is induced.

The photoinduced diode effect in the visible range has been intensively studied at room temperature [32, 33]. Several mechanisms have been proposed, e.g., the redistribution of oxygen vacancies in the electric field with the formation of a p - n junction. In single-domain films, the electric polarization of a domain can induce an asymmetric band bending at the surface [34, 35]. The influence of temperature on the induced diode effect was not investigated. According to the proposed models, this effect should vanish upon heating. In the investigated bismuth ferrite films, the effect was not observed in the near-IR range.

The aim of this study was to elucidate the mechanism of the photoinduced diode effect in the near-IR range and temperature stability.

2. X-ray diffraction and polarization

The bismuth ferrite solid solution films were formed by the burst-mode deposition of the preliminary synthesized solid solutions onto object glasses. The precursors used were powders with a grain size from 0.1 to 0.3 mm. The deposition was performed in a UVN-71P-2 vacuum facility. The pressure in a reaction chamber during deposition was 10^{-3} Pa. The tantalum evaporator temperature was kept at a level of ~ 2000 °C. The substrates were placed at a distance of 10 cm from the evaporator. The substrate temperature ranged between 250 °C–300 °C. The films were 1240-nm-thick and had geometric sizes of 13×17 mm. To measure the I - V characteristic, $\text{BiMn}_x\text{Fe}_{1-x}\text{O}_3$ films were coated with copper contacts in form of squares with a side ~ 3 mm and the distance between them was 4 mm.

The x-ray diffraction (XRD) study of the obtained $\text{BiMn}_x\text{Fe}_{1-x}\text{O}_3$ films with $X = 0.05$ and 0.15 was carried out on a DRON-3 diffractometer ($\text{CuK}\alpha$ radiation) at a temperature of 300 K after the magnetic and electric measurements (figures 1(a), (b)). The XRD data on the $\text{BiMn}_x\text{Fe}_{1-x}\text{O}_3$ thin-film compounds showed the presence of rhombohedral (sp. gr. $R3c(161)$) phase [36]. The unit cell parameters of the rhombohedral structure are $a = 0.557$ nm and $c = 1.371$ nm at $X = 0.05$ and $a = 0.558$ nm and $c = 1.387$ nm at $X = 0.15$. Reflections of low intensity impurity phases ($\sim 5\%$) of the main phase is presented on the x-ray pattern.

Using the IR spectroscopy investigations, we can establish the presence of crystal lattice defects and crystal phases

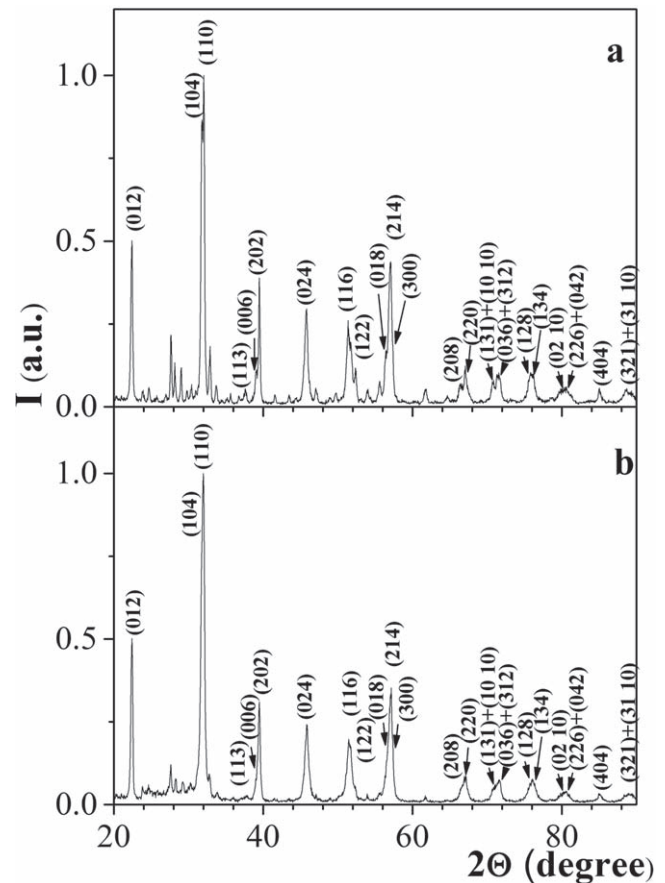


Figure 1. XRD patterns of the films $\text{BiMn}_x\text{Fe}_{1-x}\text{O}_3$ for $X = 0.05$ (a) and $X = 0.15$ (b) at $T = 300$ K.

with different symmetries. The IR absorption spectra of the polycrystalline $\text{BiMn}_x\text{Fe}_{1-x}\text{O}_3$ films were recorded on an FSM 2202 Fourier spectrometer in the frequency range of 450 – 7000 cm^{-1} . The absorption spectrum in the optical range was obtained on a Cary500Scan spectrophotometer (figure 2). For the composition with $X = 0.15$, an additional absorption was established in the near-IR range, which can be decomposed into two Lorentzians with the centers at $E_1 = 2.1$ eV and $E_2 = 4.8$ eV (figure 2(a)). The absorption with the center at E_1 corresponds to the transition of electrons from the impurity subband to the conduction band, which starts at 3 eV. For the composition with $X = 0.05$, we may distinguish one absorption band (figure 2(b)) with two boundaries for disordered semiconductors, which is caused by the Fermi levels for electrons (F^e) and holes (F^h) and the classical electron (E_c^e) and hole (E_c^h) percolation levels (figure 3). To estimate the difference $F^e - F^h$ and band gap $E_g = E_c^e - E_c^h$, which is determined as a difference between the electron and hole percolation thresholds, we use the relation for direct(indirect)-gap semiconductors [37]:

$$\alpha = \frac{A(h\nu - E_g)^{\frac{n}{2}}}{h\nu}, \quad (1)$$

where A is a parameter, $h\nu$ is the photon energy, E_g is the optical band gap energy, α is absorption coefficient, and n is the number equal to 1 for direct-gap semiconductors and 4 for

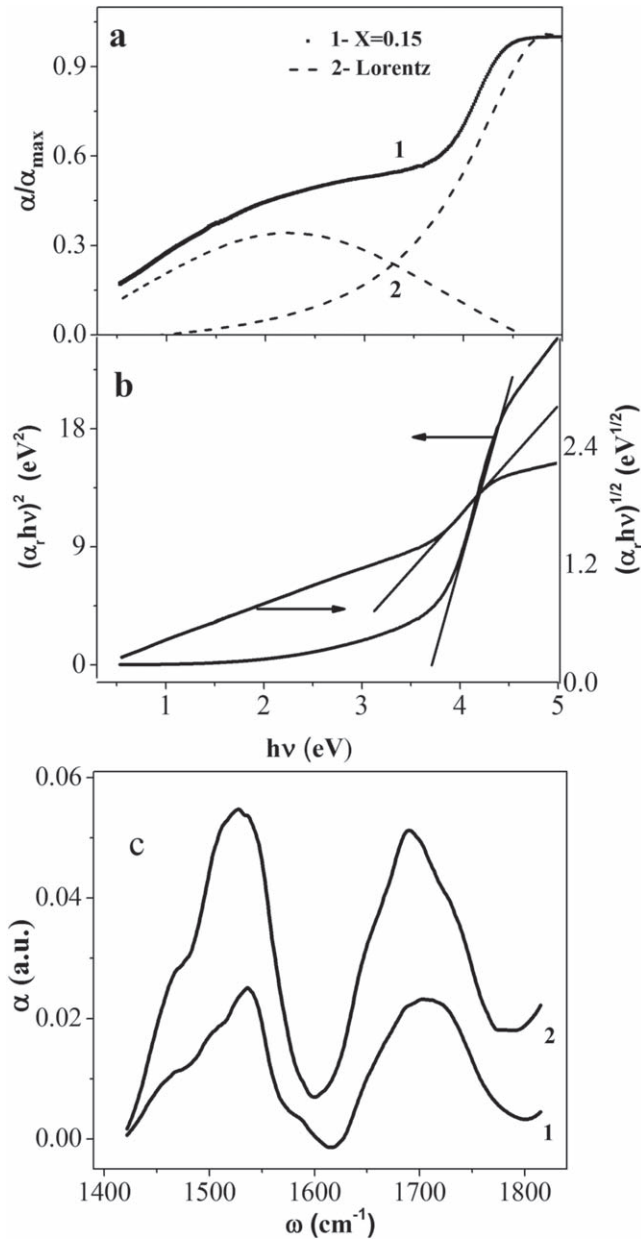


Figure 2. (a) Optical absorption for $X = 0.15$ (1) and Lorentz functions (2); (b) absorption coefficient $\alpha_r = \alpha/\alpha(h\nu = 5 \text{ eV})$ for $X = 0.05$ versus photon energy. (c) IR absorption for $X = 0.05$ (1), 0.15 (2) versus frequency (c).

indirect-gap semiconductors. The energy band gaps of the $\text{BiMn}_x\text{Fe}_{1-x}\text{O}_3$ films can be estimated from the tangent lines in the $(\alpha h\nu)^2$ versus photon energy ($h\nu$) plot for direct-gap semiconductors and $(\alpha h\nu)^{1/2}$ versus photon energy ($h\nu$) plot for indirect-gap semiconductors (figure 2(a)). The indirect gap is $\Delta E_F = F^c - F^h = 2.4 \text{ eV}$ and the energy difference between the electron and hole percolation thresholds is $(E_c^e - E_c^h) = 3.7 \text{ eV}$.

In the far-IR range below 2000 cm^{-1} , the absorption intensity abruptly drops and two maxima at frequencies of $\omega_1 = 1535$ and 1705 cm^{-1} are observed for the concentration of $X = 0.05$ (figure 2(c)). As the concentration increases, the peaks shift by $4\text{--}10 \text{ cm}^{-1}$ toward lower frequencies and the intensity doubles. According to the LDA calculations [28],

the energy levels of the oxygen vacancies in the BiFeO_3 crystal structure are about 0.1 eV . The formation of oxygen hole centers O^- and oxygen vacancies $\text{V}(\text{O}_{2-})^+$ of the F^+ -center type can occur. The crystal structure symmetry lowering will increase the crystal field and shift the defect state energy levels. The absorption at the frequencies $\omega_{1,2}$ is related to the transition of electrons from cations to the oxygen vacancy V_{O} with an energy splitting of $\Delta E = 170 \text{ cm}^{-1} = 0.022 \text{ eV}$.

The high manganese content in BFO (15%–20%) decreases the band gap of bismuth ferrite nanoparticles to 1.58 eV . According to the LDA calculation of the $[\text{Bi}_{16}(\text{Fe}_{15}\text{Mn})\text{O}_{48}]$ cluster with the rhombohedral symmetry $R3$, the impurity subband is higher than the valence band by 0.9 eV [28]. Taking into account the $3d^4$ electron configuration of Mn^{3+} ions, we found a splitting of 0.03 eV for the hybridized electron states d_{yz} and d_{zx} with $2p$ nearest oxygen ions at the point L of the Brillouin zone.

In the $\text{BiMn}_{0.05}\text{Fe}_{0.95}\text{O}_3$ film, the absorption of the electromagnetic radiation linearly grows in the energy range of $1\text{--}3 \text{ eV}$. This is due to the strong spatial fluctuations of the electric field strength in the film. The random electric field is induced near charged structural defects or ferroelectric regions with the broken local electroneutrality. In such a system, the spectrum of localized states is continuous.

The top of the valence band and the bottom of the conduction band can cross the Fermi level. In these regions, the optical transitions between the heavy and light hole bands can occur. The absorption of this type is threshold less and represents a slowly varying frequency function. The density of electronic states correlates with the light absorption coefficient. If the fluctuations of the electric field $\langle E^2 \rangle$ exceed the band gap energy and satisfy the condition [38]:

$$\sqrt{\frac{\hbar^2 e^2 \langle E^2 \rangle}{36 m_r}} > E_g, \quad (2)$$

where e is the elementary charge and m_r is the reduced electron and hole effective mass, then the absorption coefficient is a linear frequency function: $\alpha \approx \omega$. Equation (2) is valid under the condition that the ferroelectric domain has a polarization of $P \approx 10^{-6} \text{ C} \cdot \text{cm}^{-2}$ and an effective mass of $m_r = (5\text{--}1)m_e$.

The absorption spectra allow one to suggest the electron density of states. The conduction and valence band boundaries give rise to the tails of the density of states, which are caused by a random field. For the composition with $X = 0.05$, the tails originating at the band edges overlap (figure 3(a)); for the composition with $X = 0.15$, a maximum forms in the vicinity of the chemical potential (figure 3(b)). The tails of the valence and conduction bands form the donor and acceptor states. The positively and negatively charged centers induce a random Coulomb field. In a semiconductor with the random field, the bands bend (figure 3(c)). The degenerate electron and hole gas regions arise in the film. In heavily doped semiconductors, electron droplets exist [39].

We determine the presence of the electric polarization at two frequencies. For this purpose, two contacts were formed

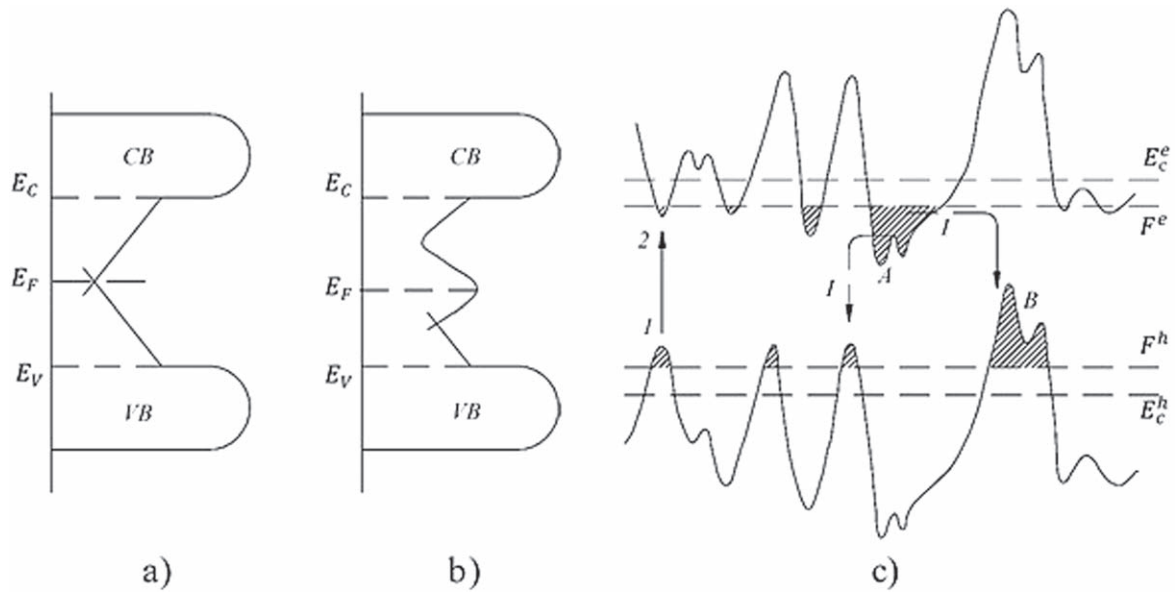


Figure 3. The electron density of states for $X = 0.05$ (a), 0.15 (b). Spatial potential fluctuations, Fermi levels for electrons F^e and holes F^h , edge of electron and hole mobility $E_{v,c}$ (c).

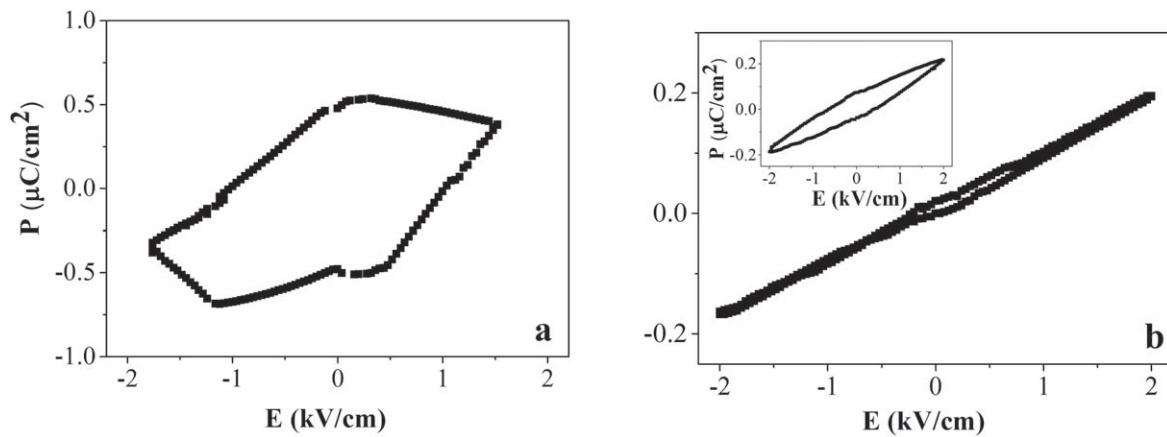


Figure 4. Polarization of the $\text{BiMn}_x\text{Fe}_{1-x}\text{O}_3$ for $X = 0.05$ (a), $X = 0.15$ (b) at $T = 80$ K versus electric field. Inset: $P(E)$ for $X = 0.15$ / $T = 380$ K.

on the film surface and a common contact was formed on the substrate. The electric voltage is applied to the contacts on the substrate and film and the current on the film-substrate contacts is measured [40]. The polarization is determined by the time integration of the pyroelectric current: $P = \int j dt$ [41]. Figure 4 shows the field dependence of the polarization for the two compositions at an ac voltage frequency of $\omega = 10$ mHz. The film with $X = 0.05$ exhibits a $P(E)$ hysteresis (figure 4(a)). The hysteresis width $\Delta P = 0.9 \mu \cdot \text{C} \cdot \text{cm}^{-2}$ and residual polarization are temperature-independent up to $T = 280$ K. Above 300 K, leakage currents arise during the polarization processing in the time interval of 0–100 s.

The hysteresis is caused by the two factors: the domain structure of ferroelectrics and localization of electrons and holes in the potential wells with the formation of a local polarization. Electrons neutralize the positive charge on the domain surface and lead to the downward band bending. On the other hand, positively charged holes near the negative

domain charge induce the upward band bending. A metal-semiconductor ferroelectric Schottky contact with the rectifying diode characteristics forms. The internal field at the Schottky contact is directed from the positively to negatively bound charge and changes its direction upon polarization variation. The ferroelectrically bound charges are not fully compensated by the electrode charges due to the interphase effects [42]. At temperatures above 340 K, the hysteresis shifts along the polarization axis due to the leakage currents.

For the composition with $X = 0.15$, there is no hysteresis below 300 K and the dielectric susceptibility is temperature-independent. Above 300 K, the hysteresis starts forming and shifting along the polarization axis (figure 4(b)) due to the leakage currents. The polarization at a frequency of $\omega = 100$ Hz for the composition with $X = 0.05$ also exhibits the hysteresis (figure 5(a)) with a residual polarization of $P_r = 1.1 \mu \cdot \text{C} \cdot \text{cm}^{-2}$. The hysteresis width decreases upon heating and under illumination of the film in the IR range above 250

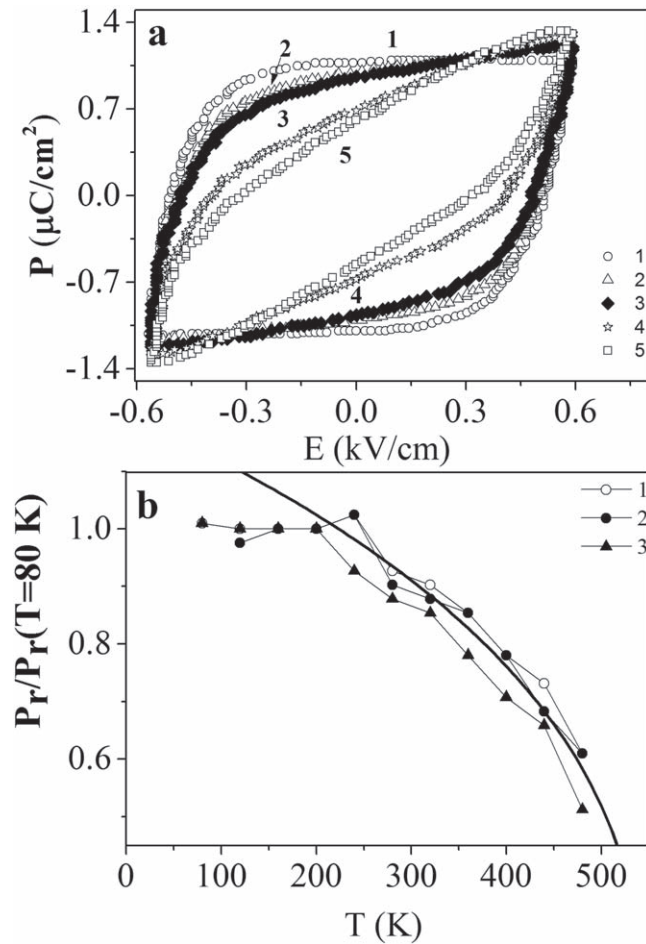


Figure 5. (a) The hysteresis of the electric polarization at frequency of $\omega = 100$ Hz for $X = 0.05$ without light (2, 4), at illumination with $\lambda = 405$ nm (1), $\lambda = 830$ nm (3, 5) at $T = 120$ K (1), $T = 320$ K (2, 3), $T = 480$ K (4,5). (b) Remnant polarization on temperature without light (1), at illumination with $\lambda = 405$ nm (2), $\lambda = 830$ nm (3).

K. The temperature dependence $P_r/P_r(T = 80 \text{ K}) = A(1 - T/T_c)^{0.35}$ is satisfactorily described by a power dependence. This process is related to a decrease in the electron contribution to the polarization due to delocalization of electrons (holes) in the potential wells. Illumination of the films leads to an increase in the number of carriers at the mobility boundary and their partial recombination. The electric polarization is related to the conductivity of the films.

3. I-V characteristics and photocurrent

We determine the diode characteristic of the photocurrent from the I - V characteristics measured under illumination at two wavelengths, $\lambda = 405$ and 830 nm, at constant temperatures (figure 6). In order to understand the mechanism of the tunable ferroelectric diode, we should clarify the conductivity mechanisms. Let us consider the three types: (i) Schottky emission caused by the electric charge accumulation at the metal-semiconductor interface, (ii) bulk conductivity with the space-charge limited current (SCLC), and (iii) bulk

Poole-Frenkel (PF) emission [43]. In the Schottky model, the field dependence of the current is

$$I \propto T^2 \exp \left[\frac{1}{k_B T} \left(\frac{e^3}{4\pi\epsilon_0\epsilon} E \right)^{0.5} \right], \quad (3)$$

where e is the elementary charge, ϵ is the permittivity, and T is the temperature. The dependence of $\ln(I)$ on $E^{1/2}$ is not linear and the Schottky model cannot be used to describe the I - V characteristic (figure 6).

The PF mechanism consists in the electric-field-driven lowering of the energy of activation of the impurity levels, which leads to an increase in the carrier density. The electrical conductivity growth with the electric field is explained by the Frenkel thermionic ionization. In this case, the current depends exponentially on the applied voltage [44]:

$$I = e\mu n_0 \frac{U}{L} \exp \frac{\beta U^{1/2}}{k_B T L^{1/2}}, \quad (4)$$

where μ is the carrier mobility, n_0 is the electron density in the conduction band in zero field, U is the applied voltage, L is the sample thickness, k_B is the Boltzmann constant, β is the PF constant, $\beta = \left(\frac{e^3}{\pi\epsilon\epsilon_0} \right)^{1/2}$, and ϵ_0 is the permittivity of vacuum. The linearity of the portions in the dependence of $\ln(I/U)$ on $U^{1/2}$ in the PF coordinates shows that the carrier transport is mainly implemented via the hopping conductivity and tunnel emission of electrons.

The I - V characteristic of the composition with $X = 0.05$ obeys the Ohm's law with the resistance decreasing with voltage U_c . This is related to the impurity states formed by manganese ions and oxygen vacancies, which will contribute to the conductivity. At low voltages, the carriers injected from the electrodes fill shallow traps. As the voltage increases ($U > U_c$), the shallow traps are filled and the transitions of electrons (holes) to the higher vacant states start contributing to the resistance. The change in the external electric field polarity also leads to the change in U_c .

For the composition with $X = 0.15$, the dependence of $\ln(I/U)$ on $U^{1/2}$ is described well by a linear function in the PF coordinates (figure 7). The film conductivity at $U \rightarrow 0$ is $\sigma \approx 2 \cdot 10^9 \Omega$; upon heating, the value smoothly grows. The PF mechanism works when the minimum distance between traps is twice as large as the distance between the trap and potential barrier maximum $r_m = \sqrt{\frac{e}{\pi\epsilon\epsilon_0 E_{cr}}}$ [45]. This condition corresponds to the trap concentration

$$N_t \approx \frac{1}{(2r_m)^2} = (\pi\epsilon\epsilon_0 E_{cr} e^{-1})^{3/2}, \quad (5)$$

where E_{cr} is the minimum electric field of the PF observation. The estimation using equation (5) at $\epsilon = 10$ yields a trap concentration of $N_t \sim 10^{16}$.

The effect of light on the I - V characteristic was studied at four illumination powers up to $0.6 \text{ W} \cdot \text{cm}^{-2}$ for the red laser and up to $0.08 \text{ W} \cdot \text{cm}^{-2}$ for the blue laser. The photocurrent $I_{ph} = I(IR) - I(0)$ as a function of voltage for the composition with $X = 0.05$ is shown in (figure 8). In the IR range, the variation in the photocurrent $\Delta I_{ph} = (I(IR) - I(0))/I(0)$ is no

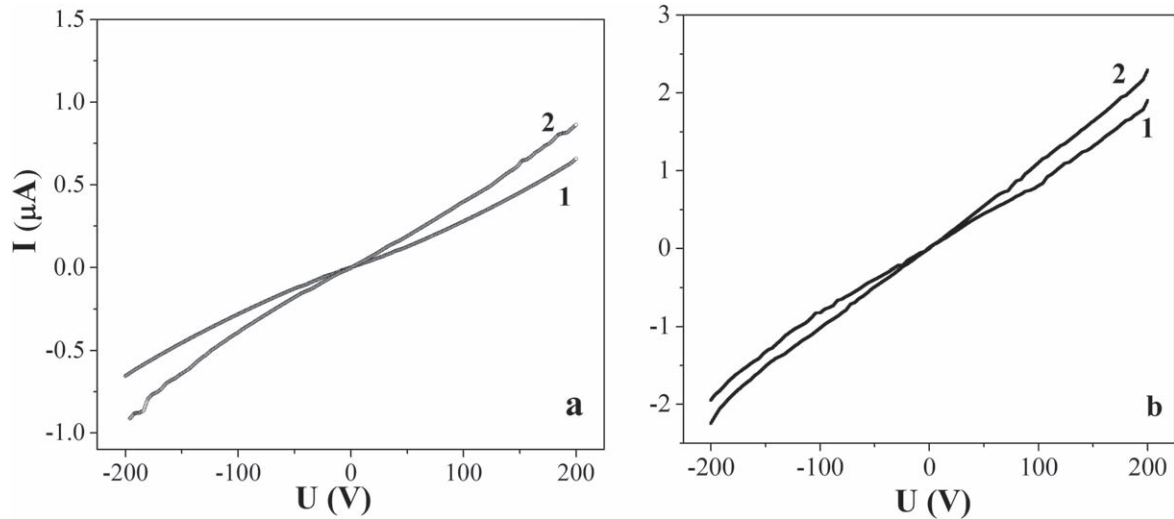


Figure 6. VAX of the $\text{BiMn}_{0.05}\text{Fe}_{0.95}\text{O}_3$ without illumination (1) and with $\lambda = 405$ nm, power $P_w = 0.08 \text{ W} \cdot \text{cm}^{-2}$ (2) at $T = 300$ K (a), $T = 390$ K (b).

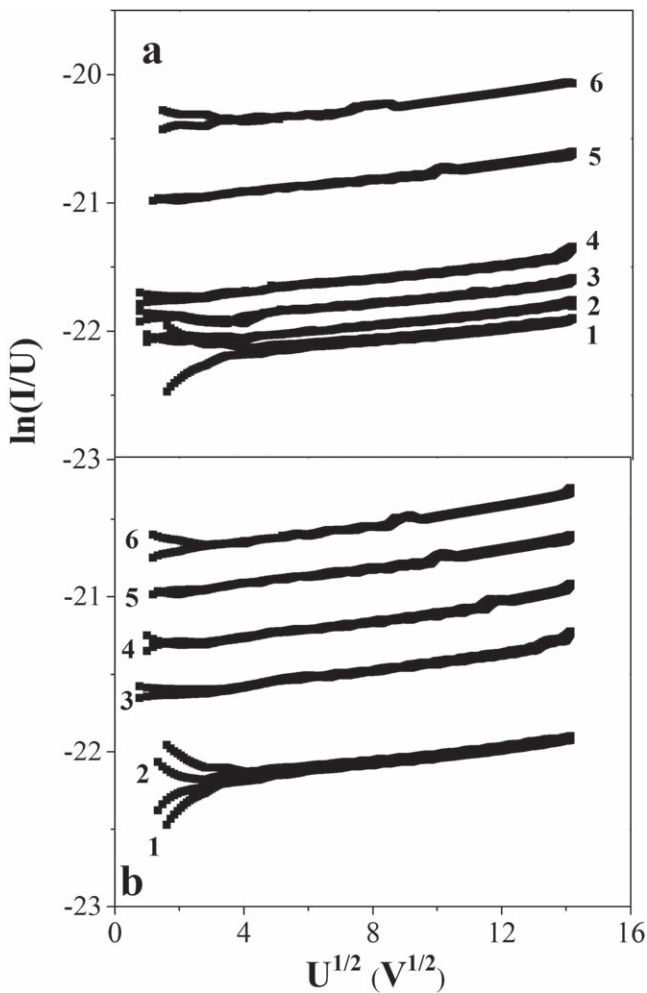


Figure 7. $\ln(I/U)$ versus $U^{1/2}$ of the $\text{BiMn}_{0.15}\text{Fe}_{0.85}\text{O}_3$ without illumination (1, 3, 5) and with $\lambda = 405$ nm, power $P_w = 0.08 \text{ W} \cdot \text{cm}^{-2}$ (2, 4, 6) (a) with illumination $\lambda = 830$ nm, $P_w = 0.6 \text{ W} \cdot \text{cm}^{-2}$ (2, 4, 6) (b) at $T = 300$ K (1, 2), $T = 340$ K (3, 4), $T = 390$ K (5, 6).

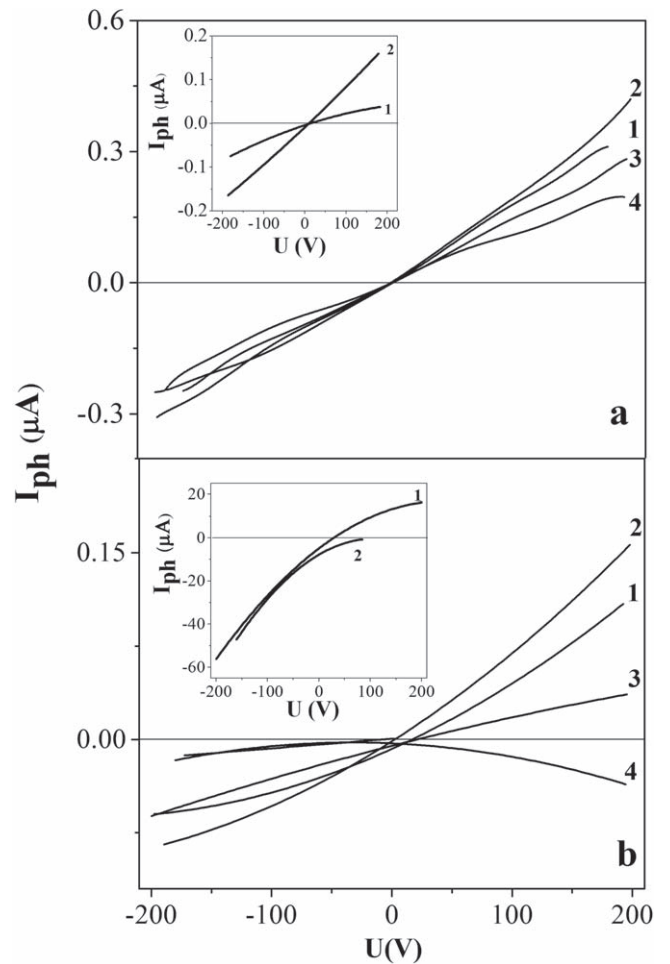


Figure 8. Photocurrent $I_{ph} = I(\text{IR}) - I(0)$ from voltage for $X = 0.05$ with illumination $\lambda = 405$ nm, $P_w = 0.015 \text{ W} \cdot \text{cm}^{-2}$ (1), $0.035 \text{ W} \cdot \text{cm}^{-2}$ (2), $0.06 \text{ W} \cdot \text{cm}^{-2}$ (3), $0.08 \text{ W} \cdot \text{cm}^{-2}$ (4) at $T = 300$ K (a), $T = 340$ K (b). Insert: $I_{ph}(U)$ with illumination $\lambda = 830$ nm, $P_w = 0.3 \text{ W} \cdot \text{cm}^{-2}$ (1), $0.6 \text{ W} \cdot \text{cm}^{-2}$ (2) at $T = 390$ K (a), $P_w = 0.06 \text{ W} \cdot \text{cm}^{-2}$ (1), $0.3 \text{ W} \cdot \text{cm}^{-2}$ (2) at $T = 340$ K (b).

larger than one per cent at $T = 300$ K. Upon heating, the photocurrent increases. In particular, at $T = 340$ K in the negative electric field the current increases to 12% and, upon variation in the field polarity, the current changes by no more than one per cent (see the inset in figure 8(b)). This behavior is typical of diodes. Let us determine the diode effect via the photocurrent variation at different external electric field polarities $\delta_d = \Delta I_{ph}(+U) - \Delta I_{ph}(-U)$. In the near-IR range, the diode effect at $T = 340$ K is $\delta_d \approx 10\%$.

The asymmetry of the photocurrent I - V characteristic depends on the illumination power and attains its maximum $\delta_d \approx 12\%$ at a power of $P_w = 0.35 \text{ W} \cdot \text{cm}^{-2}$ and $T = 390$ K. The photocurrent increases to 29% at $T = 420$ K and the diode effect is $\delta_d \approx 5\%$ at a power of $P_w = 0.18 \text{ W} \cdot \text{cm}^{-2}$. The photocurrent increases upon heating in the IR range and the diode effect attains its maximum value in the range of $T = 340$ - 390 K. Under illumination of the film at a wavelength of 405 nm, the photocurrent has a maximum at $P_w = 0.035 \text{ W} \cdot \text{cm}^{-2}$ in the temperature range of 300-390 K (figure 8).

The relative change in the current at voltages above 100 V is $\Delta I_{ph} = 65, 18,$ and 31% at temperatures of $T = 300, 340,$ and 390 K, respectively. At $T = 420$ K, the current decreases to 5% under illumination. At the change in the voltage polarity at this irradiation power, the photocurrent changes for $\delta_d \approx 15\%$ ($T = 300$ K) and decreases to $\delta_d \approx 8\%$ with an increase in the illumination power to $P_w = 0.08 \text{ W} \cdot \text{cm}^{-2}$. The diode effect attains its maximum of $\delta_d \approx 6\%$ at $P_w = 0.035 \text{ W} \cdot \text{cm}^{-2}$ and $T = 340$ K. The heating to $T = 390$ K enhances the diode effect to $\delta_d \approx (8-10)\%$ at $P_w = 0.06 \text{ W} \cdot \text{cm}^{-2}$ above $U = 150$ V.

In inhomogeneous semiconductors with the Coulomb potential fluctuation, the conductivity is determined by the position of the quasi-Fermi levels for electrons and holes relative to the carrier mobility edge (figure 3(c)). Under irradiation in the IR spectral range, electrons pass from the hole- to electron-type wells (transition 1-2 in figure 3(c)), where they tunnel to the nearest well. The quantum effects depend on the scale and amplitude of the Coulomb potential fluctuations. If the photon energy is higher than the gap energy, then nonequilibrium electrons in the conduction band are collected in the minima of the potential relief (region A) and nonequilibrium holes are collected in the maxima (region B). This process can occur under the condition that the thermalization of nonequilibrium holes and electrons in the bands occurs faster than their recombination. As a result, electrons and holes are spatially separated and the recombination significantly slows down. Under illumination, the conductivity increases if the recombination activation energy is higher than the conductivity activation energy, i.e., than the energy necessary to throw carriers to the percolation level, which is observed under illumination of the film by the blue laser. As the phonon pumping increases, the recombination (e.g., transition I figure 3(c)) enhances, which leads to a decrease in the density of states at the mobility level and in the current. The diode effect is related to the asymmetry of the quantum well due to the presence of electric polarization in the film. If the external electric field is co-directed with the polarization,

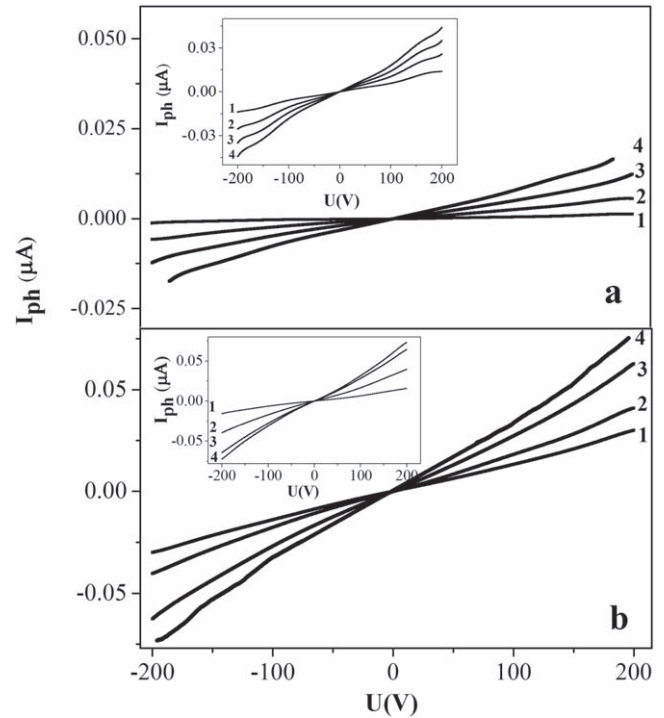


Figure 9. Photocurrent $I_{ph} = I(\text{IR}) - I(0)$ from voltage for $X = 0.15$ with illumination $\lambda = 405$ nm, $P_w = 0.015 \text{ W} \cdot \text{cm}^{-2}$ (1), $0.035 \text{ W} \cdot \text{cm}^{-2}$ (2), $0.06 \text{ W} \cdot \text{cm}^{-2}$ (3), $0.08 \text{ W} \cdot \text{cm}^{-2}$ (4) at $T = 340$ K (a), $T = 390$ K (b). Inset: $I_{ph}(U)$ with illumination $\lambda = 830$ nm, $P_w = 0.06 \text{ W} \cdot \text{cm}^{-2}$ (1), $0.15 \text{ W} \cdot \text{cm}^{-2}$ (2), $0.3 \text{ W} \cdot \text{cm}^{-2}$ (3), $0.6 \text{ W} \cdot \text{cm}^{-2}$ (4) at $T = 340$ K (a), $T = 390$ K (b).

then the photoelectrons localized at the mobility level are accumulated in a deeper quantum well. The asymmetry of wells changes with the field polarity.

In the field with the high manganese concentration ($X = 0.15$), the impurity band from manganese ions forms, which consist of the quasi-periodic potential wells. The top of the valence band and the bottom of the conduction band change in the space and the bands are smoothly bent due to structural defects and oxygen vacancies. The I - V characteristic of the photocurrent is shown in (figure 9). Under illumination of the film by light quanta with an energy of $h\nu = 3$ eV, the dominant carriers are holes in the valence bands and electrons in the conduction bands. The photocurrent decreases by an order of magnitude with increasing concentration due to the disappearance of the electric polarization. The dependence of the current on the blue laser radiation intensity is linear (figure 10) and proportional to the density of carriers that passed from the valence to conduction band upon absorption of a photon. At room temperature, the deviation from the linear dependence and a slight change in the photocurrent with power originate from the subband curvature fluctuation and larger carrier thermalization time as compared with the recombination time. The photocurrent asymmetry is not observed and the diode effect with $\delta_d = 3\%$ occurs at $T = 420$ K under illumination at a radiation power of $P_w = 0.08 \text{ W} \cdot \text{cm}^{-2}$. Under weak illumination of the film, the diode effect did not found.

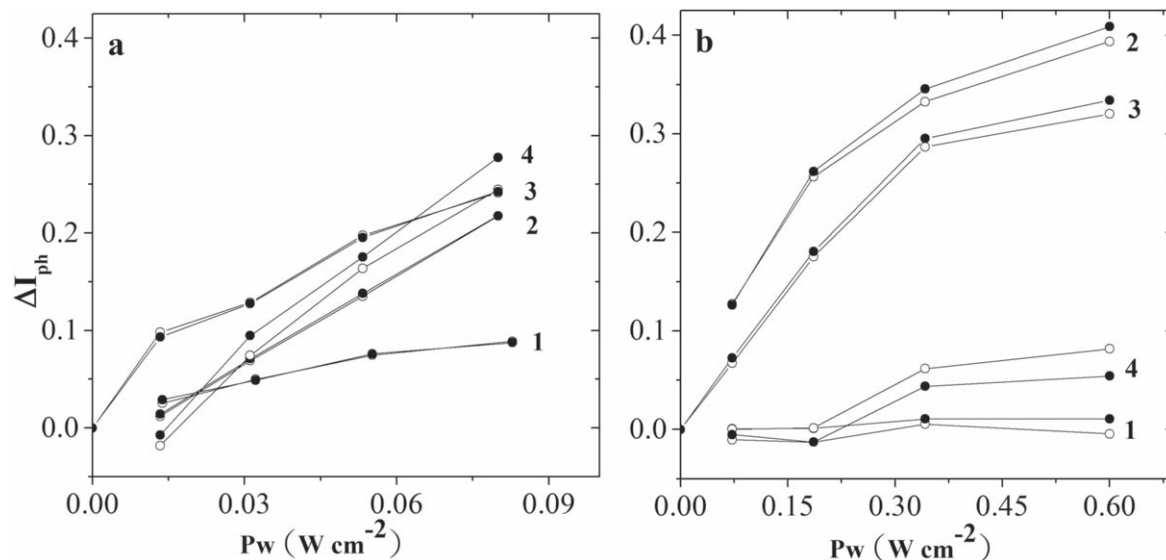


Figure 10. Relative change of photocurrent $I_{ph} = (I(IR) - I(0))/I(0)$ versus radiation intensity $U = -150\ V$ (open symbols) and $U = 150\ V$ (black symbols) for $X = 0.15$. (a) with $\lambda = 405\ nm$, $T = 300\ K$ (1), $T = 340\ K$ (2), $T = 390\ K$ (3), $T = 420\ K$ (4); (b) with $\lambda = 830\ nm$, $T = 300\ K$ (1), $T = 340\ K$ (2), $T = 390\ K$ (3), $T = 420\ K$ (4).

In the near-IR range, the photocurrent is no higher than $\Delta I_{ph} = 2\%$ at $T = 300\ K$ (figure 10). Upon heating, the photocurrent smoothly increases and passes to the saturation at $T = 340$ and $390\ K$. With a further increase in the temperature, the photocurrent decreases. The maximum in the temperature dependence of the photocurrent is related to the maximum mobility of electrons and holes. In this case, the thermalization of carriers occurs faster than their recombination. The photocurrent saturation is caused by the electron depletion near the chemical potential in the impurity subband. The existence of potential wells is confirmed by the I - V characteristic, the behavior of which is due to electron hoppings over the potential wells and obeys the PF law. The photocurrent asymmetry at the electric field polarity change (the diode effect) is no larger than 2% in the IR range.

4. Conclusions

For the $BiMn_xFe_{1-x}O_3$ film composition with $X = 0.05$, the optical absorption intensity was found to linearly increase with frequency in the band gap, which is caused by the strong Coulomb potential fluctuation. For this composition, the direct and indirect gaps were observed, which are related to the transition of electrons from the states below the Fermi level of holes to the state above the Fermi level of electrons near the conduction band. For the film composition with $X = 0.15$, there is an impurity subband formed by manganese ions, which is consistent with the LDA data. In the $BiMn_xFe_{1-x}O_3$ films with $X = 0.05$, the electric polarization hysteresis was found, which is absent in the films with $X = 0.15$. The film conductivity obeys the Ohm's law at $X = 0.05$ and the Poole-Frenkel law at $X = 0.15$. The dependence of the photocurrent on the illumination intensity at two wavelengths in the violet and IR spectral ranges was established. It was demonstrated that under illumination at a

wavelength of 405 nm, the photocurrent passes through its maximum at $X = 0.05$ and smoothly grows at $X = 0.15$ with the illumination intensity. In the IR range, the photocurrent saturates. The temperature and concentration dependences of the diode effect in the near-IR and violet ranges for the $BiMn_xFe_{1-x}O_3$ film were determined. The diode effect was shown to be caused by the quantum well asymmetry due to the electric polarization in the film, band bending at the film surface, and filling of the quantum wells by electrons and holes because of the difference between the times of carrier thermalization and recombination of electrons and holes.

Acknowledgments

The reported study was funded by RFBR according to the research project №18-52-00009 Bel_a; № 18-32-00079 mol_a and Belarusian Foundation project № F18R-084. The reported study was funded by Russian Foundation for Basic Research, Government of Krasnoyarsk Territory, Krasnoyarsk Regional Fund of Science № 18-42-240001 r_a, to the research project: «Inversion of the sign of the components of the magnetoelectric tensor on the temperature in films of bismuth garnet ferrite replaced by neodymium». This work is part of the research program the state order № 3.5743.2017/6.7.

ORCID iDs

S S Aplesnin <https://orcid.org/0000-0001-6176-4248>
O B Romanova <https://orcid.org/0000-0002-7883-3702>

References

- [1] Paillard C, Bai X, Infante I C, Guennou M, Geneste G, Alexe M, Kreisel J and Dkhil B 2016 Photovoltaics with ferroelectrics: current status and beyond *Adv. Mater.* **28** 5153
- [2] Seidel J and Eng L M 2014 Shedding light on nanoscale ferroelectrics *Curr. Appl. Phys.* **14** 1083
- [3] Meier D, Seidel J, Cano A, Delaney K, Kumagai Y, Mostovoy M, Spaldin N A, Ramesh R and Fiebig M 2012 Anisotropic conductance at improper ferroelectric domain walls *Nat. Mater.* **11** 284
- [4] Yuan Y, Xiao Z, Yang B and Huang J 2014 Arising applications of ferroelectric materials in photovoltaic devices *J. Mater. Chem. A* **2** 6027
- [5] Pyatakov A P and Zvezdin A K 2012 Magnetolectric and multiferroic media *Physics—Uspekhi* **55** 557
- [6] Småbråten D R, Meier Q N, Skjærø S H, Inzani K, Meier D and Selbach S M 2018 Charged domain walls in improper ferroelectric hexagonal manganites and gallates *Phys. Rev. Mater.* **2** 114405
- [7] Seidel J et al 2009 Conduction at domain walls in oxide multiferroics *Nat. Mater.* **8** 229
- [8] Fiebig M, Lottermoser T, Fröhlich D, Goltsev A V and Pisarev R V 2002 Observation of coupled magnetic and electric domains *Nature* **419** 818
- [9] Lin Y-H, Ying M, Li M, Wang X and Nan C-W 2007 Room-temperature ferromagnetic and ferroelectric behavior in polycrystalline ZnO-based thin films *Appl. Phys. Lett.* **90** 222110
- [10] Catalan G and Scott J F 2009 Physics and applications of bismuth ferrite *Adv. Mater.* **21** 2463
- [11] Ravindran P, Vidya R, Kjekshus A, Fjellvåg H and Eriksson O 2006 Theoretical investigation of magnetoelectric behavior in BiFeO₃ *Phys. Rev. B* **74** 224412
- [12] Sosnowska I, Neumaier T P and Steichele E 1982 Spiral magnetic ordering in bismuth ferrite *J. Phys. C: Sol. Stat. Phys.* **15** 4835
- [13] Yang M-M, Bhatnagar A, Luo Z-D and Alexe M 2017 Enhancement of local photovoltaic current at ferroelectric domain walls in BiFeO₃ *Nat. Sci. Reports* **7** 43070–8
- [14] Yang S Y et al 2010 Above-bandgap voltages from ferroelectric photovoltaic devices *Nat. Nanotechnol.* **5** 143
- [15] Zhao T et al 2006 Electrical control of antiferromagnetic domains in multiferroic BiFeO₃ films at room temperature *Nat. Mater.* **5** 823
- [16] Eliseev E A, Morozovska A N, Svechnikov G S, Maksymovych P and Kalinin S V 2012 Domain wall conduction in multiaxial ferroelectrics *Phys. Rev. B* **85** 045312
- [17] Bhatnagar A, Chaudhuri A R, Kim Y H, Hesse D and Alexe M 2013 Role of domain walls in the abnormal photovoltaic effect in BiFeO₃ *Nat. Comm.* **4** 2835
- [18] Cherian J G, Turan B, Harms N C, Gao B, Cheong S-W, Vanderbilt D and Musfeldt J L 2016 Optical spectroscopy and band gap analysis of hybrid improper ferroelectric Ca₃Ti₂O₇ *Appl. Phys. Lett.* **108** 262901
- [19] Panda B, Dhar A, Nigam D, Bhattacharya D and Ray K 1998 Optical properties of RF sputtered strontium substituted barium titanate thin films *Thin Solid Films* **332** 46
- [20] Ihlefeld J F et al 2008 Optical band of BiFeO₃ grown by molecular-beam epitaxy *Appl. Phys. Lett.* **92** 142908
- [21] Basu S R, Martin L W, Chu Y H, Gajek M, Ramesh R, Rai R C, Xu X and Musfeldt J L 2008 Photoconductivity in BiFeO₃ thin films *Appl. Phys. Lett.* **92** 091905
- [22] Grinberg I et al 2013 Perovskite oxides for visible-light-absorbing ferroelectric and photovoltaic materials *Nature* **503** 509
- [23] Nechache R, Harnagea C, Li S, Cardenas L, Huang W, Chakrabarty J and Rosei F 2015 Bandgap tuning of multiferroic oxide solar cell *Nat. Photonics* **9** 61
- [24] Butler K T, Frost J M and Walsh A 2015 Ferroelectric materials for solar energy conversion: photoferroics revisited *Energy Environ. Sci.* **8** 838
- [25] Zhai J, Zhang X'an, Hai F S, Yu X, Zhu R and Zhang W 2014 Fabrication and characterization of the thin-film transistors with SnO₂ channel by spray pyrolysis *Jpn. J. Appl. Phys.* **53** 066506
- [26] Zhao J W, Zhang X A, Li S, Zheng H W, Yang G and Zhang W F 2017 Performances of transparent indium zinc oxide thin film transistor using ZrO₂ as dielectric processed by solution method *Phys. Status Solidi A* **214** 1600315
- [27] Zhu R, Zhang X A, Zhao J W, Li R P and Zhang W F 2015 Influence of illumination intensity on the electrical characteristics and photoresponsivity of the Ag/ZnO Schottky diodes *J. Alloys Compd.* **631** 125
- [28] Matsuo H, Noguchi Y and Miyayama M 2017 Gap-state engineering of visible-light-active ferroelectrics for photovoltaic applications *Nat. Comm.* **8** 207
- [29] Peng L, Deng H, Ren Q, Tian J, Ren Q, Peng C, Huang Z, Yang P and Chu J 2013 Influence of Co doping on structural, optical and magnetic properties of BiFeO₃ films deposited on quartz substrates by sol-gel method *Appl. Surf. Sci.* **268** 146
- [30] Xu X, Ihlefeld J F, Lee J H, Ezekoye O K, Vlahos E, Ramesh R, Gopalan V, Pan XQ, Schlom DG and Musfeldt J L 2010 Tunable band gap in Bi(Fe_{1-x}Mn_x)O₃ films *Appl. Phys. Lett.* **96** 192901
- [31] Huan W, Cheng C, Yang Y, Yuan H and Li Y 2012 A study on the magnetic and photoluminescence properties of Eu(n⁺) and Sm³⁺ doped Fe₃O₄ nanoparticles *J. Nanosci. Nanotechnol.* **12** 4621
- [32] Jiang A Q, Wang C, Jin K J, Liu X B, Scott J F, Hwang C S, Tang T A, Lu H B and Yang G Z 2011 A resistive memory in semiconducting BiFeO₃ thin-film capacitors *Adv. Mater.* **23** 1277
- [33] Wang C, Jin K-J, Xu Z-T, Wang L, Ge C, Lu H-B, Guo H-Z, He M and Yang G-Z 2011 Switchable diode effect and ferroelectric resistive switching in epitaxial BiFeO₃ thin films *Appl. Phys. Lett.* **98** 192901
- [34] Choi T, Lee S, Choi Y J, Kiryukhin V and Cheong S W 2009 Switchable ferroelectric diode and photovoltaic effect in BiFeO₃ *Science* **324** 63
- [35] Lee D, Baek S H, Kim T H, Yoon J-G, Folkman C M, Eom C B and Noh T W 2011 Polarity control of carrier injection at ferroelectric/metal interfaces for electrically switchable diode and photovoltaic effects *Phys. Rev. B* **84** 125305
- [36] Graf M E, Napoli S D, Barral M A, Saleh Medina L M, Negri R M, Sepiarsky M and Llois A M 2018 Rhombohedral R3 to orthorhombic Pnma phase transition induced by Y-doping in BiFeO₃ *J. Phys.: Condens. Mat.* **30** 285701
- [37] Pankove J N 1971 *Optical Processes in Semiconductors* (New Jersey, Prentice-Hall: Published by Englewood Cliffs) p 422
- [38] Bonch-Bruевич V L and Kalashnikov S G 1977 *Semiconductor Physics* (Moscow: Nauka) p 674
- [39] Shklovsky B I and Efros A L 1984 *Electronic Properties of Doped Semiconductors* (Berlin Heidelberg: Publisher by Springer-Verlag) p 388
- [40] Rivera J-P 2009 A short review of the magnetoelectric effect and related experimental techniques on single phase (multi-) ferroics *Eur. Phys. J. B* **71** 299
- [41] Shut V N 2013 Ferroelectrics with composition gradient: On the nature of hysteresis loop shift *Phys. Sol. State* **55** 1438
- [42] Stengel M, Vanderbilt D and Spaldin N 2009 Enhancement of ferroelectricity at metal-oxide interfaces *Nat. Mater.* **8** 392

- [43] Sze S M and Kwok K N 2007 *Physics of Semiconductor Devices* (Hoboken, New Jersey: Wiley) p 763
- [44] Connell G A, Camphausen D L and Paul W 1972 Theory of poole-frenkel conduction in low-mobility semiconductors *Philos. Mag.* **26** 541
- [45] Hill R M 1971 Poole-frenkel conduction in amorphous solids *Philos. Mag.* **23** 59